VELOCITY-ESTIMATION IMPROVEMENTS AND MIGRATION/DEMIGRATION USING CRS WITH CONTINUING DECONVOLUTION IN THE TIME DOMAIN

M. Glöckner, S. Dell., C. Vanelle, and D. Gajewski

email: *martina.gloeckner@uni-hamburg.de*
keywords: *time de/migration, velocity analysis, LSM*

ABSTRACT

To obtain an image of the earth's subsurface, time-imaging methods can be applied, as they are reasonably fast, less sensitive to velocity model errors than depth-imaging methods and, usually, easy to parallelize. A powerful tool for time-imaging consists of a series of prestack time-migrations and demigrations. We apply multi-parameter stacking techniques to obtain an initial time-migration velocity model. The velocity model building proposed here is based on the kinematic wavefield attributes of the common-reflection surface method. A subsequent refinement of the velocities uses a coherence filter which is based on a predetermined threshold, and followed by an interpolation and smoothing. Then, we perform a migration deconvolution to obtain the final time-migrated image. The migration deconvolution consists of one iteration of least-squares migration with an estimated Hessian. We estimate the Hessian by non-stationary matching filters, i.e., in a data-driven fashion. The model building uses the framework of the common-reflection-surface , and the migration deconvolution is fully automated. Therefore, minimal user interaction is required to carry out both the velocity model refinement and the image update. We apply the suggested approaches of velocity refinement and migration deconvolution to complex synthetic and field data.

INTRODUCTION

Time migration is an attractive tool to produce subsurface images because it is reasonably fast, less sensitive to the model errors than depth migration and, usually, a massively parallelized technique. A highly focused time image is, however, achievable only with sufficiently well-determined migration velocities. Thus, a refinement of the initial time-migration velocities is often applied to obtain an improved final image. Also, time migration is derived by considering many assumptions, among others a straight ray propagation, regularly sampled seismic data and an infinite migration aperture. However, these assumptions are violated when sufficiently complex subsurface structures and field data are considered. Thus, time-migrated images usually suffer from imperfections of the operator, exhibiting artifacts (Hertweck et al., 2003), such as the commonly observed migration swings. Conventionally, a residual moveout (RMO) analysis is used to reduce the impact of the model errors on the image, (e.g., Yilmaz (2001). The RMO analysis is an iterative approach to update velocities based on the analysis of the flattening of events in the common-image gathers (CIG) after time migration. Another approach to perform the velocity update after prestack time-migration is common-offset migration followed by application of inverse normal moveout (NMO) and subsequent velocity analysis on the newly generated gathers. The obtained gathers contain time-migrated reflections with approximately hyperbolic moveout and are therefore suitable for classical one-dimensional or multi-dimensional velocity analysis (Dell et al., 2012). To reduce migration artifacts, several image-enhancement techniques, e.g., dip- or structure-oriented filters, are usually applied after time migration. These methods, however, can introduce a certain smoothing into the migrated images, which may increase uncertainties in

fault interpretation.

A comprehensive imaging theory based on migration and demigration in the depth domain is presented by Hubral et al. (1996) and Tygel et al. (1996). In their work, Huygens surfaces and isochrons form the central ingredients, and are combined with proper amplitude weighting to preserve amplitudes. Similar to the works mentioned above, Iversen et al. (2012) presented a time-based approach. They used reflection times, slopes, and curvatures as parameters to perform migration and demigration. Here, we propose a technique to solve both time-migration problems mentioned earlier, i.e., migration artifacts and velocity analysis. Our method is based on the duality of modeling/imaging operators (see Claerbout et al., 1996). For one thing, time migration can be achieved by summation over traces (amplitude stacking) which aims to focus events, correct dips, unfold triplications, and collapse diffractions. Following Yilmaz (2001), a corresponding migration operator can be described by a double-square-root equation. While for the other thing, time demigration can be carried out by performing a semicircle superposition (amplitude spreading) which aims to restore (model) seismic data based on provided reflectivity models. The smearing (demigration) of the amplitudes can be described by a single-square-root equation. In this case, we use the same traveltimes for both steps. The advantage of the cascaded forward and backward transformation is data enhancement and regularization due to the incorporated summation of the migration, which reduces noise. Furthermore, a general conflicting dip handling is naturally incorporated in the migration process. On the one hand, a correctly migrated image should not contain conflicting dips with the exception of multiples. On the other hand, the demigration reconstructs the dips in the original unmigrated domain. A condition to perform these steps is a suitable velocity model, which can be automatically generated via, e.g., the common-reflection-surface (CRS) method (Jäger et al., 2001).

In the first part of the paper, we suggest an efficient strategy to calculate an original starting velocity model and introduce a refinement of the migration velocities. The method utilizes kinematic wavefield attributes of the CRS method, i.e., angles and curvatures of wavefronts (Hubral, 1983) and also uses a coherence filtering of the velocities, which further conditions the final velocity model for migration. In the second part, we describe the migration and demigration in terms of traveltimes. Furthermore, we briefly review the theory of least-squares migration and show that our time-migration/demigration approach can also be used for migration deconvolution. To do this, we estimate matching filters, which are convolved with the migrated image to enhance image quality. Finally, we demonstrate the applicability of the suggested fully automated workflow for complex synthetic and field-data examples.

CONCEPTUAL FRAMEWORK

Automatic velocity model building using CRS

We perform a multidimensional coherence analysis using the implicit CRS method (Vanelle et al., 2010) to extract kinematic wavefield attributes (Hubral, 1983). In principle, any double-square-root (DSR) expression (e.g., Walda et al., 2017) can be used instead of implicit CRS. An automated local coherence analysis employing the normalized semblance coefficient (Neidell and Taner, 1971) picks at every data point a subset of CRS attributes, and determines by optimization the best set consistent with the data (Nelder and Mead, 1965). The obtained kinematic wavefield attributes are described as different order terms of a Taylor series expansion of the squared hyperbolic traveltime (Müller, 1999):

$$t^2(\Delta x, \Delta h) = (t_0 + p\Delta x)^2 + 2t_0(N\Delta x^2 + M\Delta h^2) \quad . \tag{1a}$$

$$p = \left.\frac{\partial t}{\partial x}\right|_{x_0,h_0} \quad , \quad N = \left.\frac{\partial^2 t}{\partial x^2}\right|_{x_0,h_0} \quad , \quad M = \left.\frac{\partial^2 t}{\partial h^2}\right|_{x_0,h_0} \tag{1b}$$

$$p = \frac{2\sin\alpha}{v_0}, \quad , \quad M = \frac{\cos^2\alpha}{v_0 R_{NIP}} \quad , \quad N = \frac{\cos^2\alpha}{v_0 R_N} \tag{1c}$$

The displacement between the point under consideration (x_m, h) ,denoting midpoint and half-offset, and a central point (x_0, h_0) is $\Delta x = x_m - x_0, \Delta h = h - h_0$. The traveltime at the expansion point x_0, h_0 is denoted by t_0 and the derivatives are $p, M,$ and N. The near-surface velocity v_0 has to be provided. An exploding-reflector experiment can be used to illustrate the physical meaning of the CRS attributes (see Figure 1). The angle α denotes the incidence angle of the emerging ray from a fictitous source at

the normal-incident-point (NIP). R_{NIP} is the radius of curvature of the emerging wavefront at the surface from a point source at NIP. R_N is the radius of curvature of the emerging wavefront at the surface of an exploding-reflector segment around NIP. Then, α, R_{NIP} and R_N, extracted by local coherence analysis
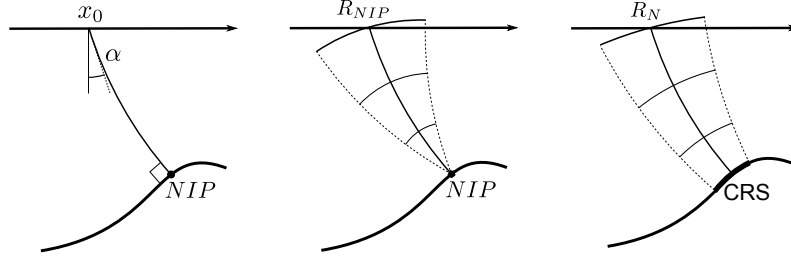
Figure 1: Kinematic wavefield attributes (modified after Schwarz et al. (2014)). A wave originates at the normal-incident point (NIP) and strikes the recording surface at the central zero-offset point x_0 with the emergence angle α. The radius of wavefront curvature of the NIP wave at the surface is R_{NIP}. The same applies for a wave starting at the CRS, and can be measured at the surface as radius of wavefront curvature of normal (N) wave R_N.

are used to calculate the initial (original) time-migration velocities (Schwarz et al., 2014):

$$V = \frac{v_{NMO}}{\sqrt{1 + \frac{v_{NMO}^2}{v_0^2} \sin^2 \alpha}} \quad \text{with} \quad v_{NMO} = \sqrt{\frac{2v_0 R_{NIP}}{t_0 \cos^2 \alpha}} \, . \tag{2}$$

In total, the migration velocity V depends on four parameters: α, R_{NIP}, the considered time t_0, and the velocity near the surface v_0, and V is calculated for every time sample and common-midpoint. As we also consider the incidence angle α, we directly obtain dip-corrected migration velocities. Furthermore, equation 2 determines the normal moveout (NMO) velocity, v_{NMO}. The near-surface velocity is an important component of the migration velocity and the choice of its locally constant value is usually based on a priori information. However, the formulation of migration velocity as in equation 2 allows a near-surface velocity scan. This is an attractive complementary benefit of equation 2, particularly for data acquired in regions with very complex near-surface geology, e.g., in deserts. As a new step, we apply a coherence filter to the obtained velocity field. We perform a coherence analysis similar to the one mentioned above to obtain the semblance for the migrated image. Therefore, the semblance coefficient (equation 3) is calculated for every sample. It is normally described as normalized ratio of output energy to input energy (Neidell and Taner, 1971).

$$S = \frac{\sum\limits_{i=1}^{M} \left(\sum\limits_{j=1}^{N} a_{ij} \right)^2}{N \sum\limits_{i=1}^{M} \sum\limits_{j=1}^{N} a_{ij}^2}, \tag{3}$$

where M is the number of samples per trace, N is the number of traces, and a is the amplitude of the i'th sample and j'th trace. The coefficient has values between zero (low accordance) and one (high accordance) due to the normalization. The amplitude for the sample under consideration depends on the migration velocity. High coherence values implicate appropriate migration velocities for this sample. In contrast to the local coherence analysis for the stacking described above, no optimization is performed, because we suppose that with the previously determined kinematic wavefield attributes an appropriate velocity is calculated. This leads to general smaller values of the migrated coherence in contrast to coherence obtained after stacking. The migrated coherence is calculated during the normal migration and is available afterwards for the velocity refinement. With the new generated attribute, we can define a threshold for the coherence that depends on the data set under consideration to eliminate noise and weak events. Only velocity values with sufficiently high semblance norm are considered for the construction of the refined velocity model. Subsequently, gaps arising from this thresholding are filled by interpolation. We use an interpolation method based on a least-squares approach, where a discrete Laplacian is used to fill the gaps. Known values are not

modified with this interpolation. Afterwards, we smooth the interpolated model to obtain a smooth velocity distribution, which is necessary for time migration. As a result, areas with large coherence imply a reliable migration velocity and the subsequent interpolation connects these areas to obtain an improved migration velocity model. Furthermore, diffractions are enhanced in the suggested strategy, because they are naturally described by the used migration equation (introduced in the next subsection), whereas reflection events are merely repositioned. The migration method is designed to emphasize diffractions by summing their energy along the whole hyperbola, whereas reflections only sum over a relatively small contribution on the apex of the hyperbola. Although amplitudes of reflections are higher, coherence values of diffractions are increased a lot with this method. The procedure can be applied iteratively in such a way that the interpolated model is used again for coherence filtering, but our tests revealed that this just leads to further smoothing without improving the velocity information.

Migration and demigration with CRS

Generally, geophysical modeling uses linear operators that predict data from models (Claerbout et al., 1996). The inverse of modeling, inversion, aims to find models from the data and also uses linear operators. The modeling operator with respect to reflectivity is conventionally referred to as demigration. The inverse, in turn, is referred to as true-amplitude migration operator. In this paper, we formulate the time-migration and demigration based on a high-order paraxial traveltime approximation. We use implicit CRS (Schwarz et al., 2014), as it belongs to the DSR equations. As the implicit CRS method is developed to perform local coherence analysis and stacking, it is parametrized by the two-way traveltime along the central zero-offset ray . To apply it for time-migration, we rewrite the implicit CRS traveltime in terms of apex coordinates (x_{apex}, t_{apex}). These are defined by local coordinates of implicit CRS (see Appendix). We re-parametrize the diffraction subset of the implicit CRS in terms of apex coordinates:

$$t = \sqrt{\frac{t_{apex}^2}{4} + \frac{(\Delta x_a - h)^2}{V^2}} + \sqrt{\frac{t_{apex}^2}{4} + \frac{(\Delta x_a + h)^2}{V^2}}, \qquad (4)$$

where $\Delta x_a = x_m - x_{apex}$ is the midpoint displacement, h is the half-offset, V is the time-migration velocity from equation 2 (Gloeckner et al., 2016). This DSR expression 4 resembles a conventional Kirchhoff migration traveltime expression (Yilmaz and Claerbout, 1980) and represents the summation in our cascaded approach of migration and demigration. In equation 4, the traveltime t is expressed as a function of apex time t_{apex} and lateral deviation from the apex location Δx_a. To obtain the corresponding demigration expression, we find it convenient to solve equation 4 for t_{apex}:

$$t_{apex} = \sqrt{t^2 - \frac{4(\Delta x_a^2 + h^2)}{V^2} + \frac{16\Delta x_a^2 h^2}{t^2 V^4}}, \qquad (5)$$

which is a single-square-root expression and represents the smearing in our cascaded approach. Both processes, migration and demigration, are likewise valid for the poststack case, where the half offset h vanishes and the equations simplify.

Migration deconvolution

Seismic time migration aims to map recorded data into a structural image of the earth's discontinuities. However, complex geological settings along the raypaths, uneven illumination, and imperfect acquisition with irregular surface sampling, finite recording aperture, and aliased seismic data frequently lead to seismic images which are improperly recovered by migration techniques. The migrated events appear to lose high frequencies, reveal decreased amplitudes, are erroneous in terms of shape and location, and exhibit migration swings. As a result, least-squares migration (LSM) techniques have been proposed to achieve a better matching of amplitudes in the migrated images (Schuster, 1993; Nemeth et al., 1999). The basic idea of the LSM techniques is to exploit the migration/demigration operator duality. In operator notation it reads:

$$d = Lm \,, \tag{6a}$$

$$m = L^{-1}d \,, \tag{6b}$$

where d are the seismic data, m is the reflectivity model (migration image), L is the linear modeling operator, and L^{-1} is the inverse (true-amplitude migration) operator. Usually, adjoint (transposed) instead of inverse operators are used for migration as they tolerate data imperfections and do not demand that the data provide full information (Claerbout et al., 1996).

The operator duality expressed in equation 6 allows us to formulate migration as a least-squares problem. If we consider the functional

$$J(m) = \frac{1}{2} \left(Lm - d \right)^2 \,, \tag{7}$$

we immediately see that the gradient $\nabla_m J$ yields the least-squares estimate of the reflectivity model

$$\frac{\partial J}{\partial m} = 0 \implies \hat{m} = (L'L)^{-1}L'd \,, \tag{8}$$

where we use the adjoint operator L' instead of the inverse operator L^{-1}. The quantity $(L'L)^{-1}$ in equation 8 represents the Hessian and $\hat{m}$ denotes the improved migrated image. In the literature, this inverse is frequently referred to as the resolution matrix or deconvolution operator (Hu et al., 2001), i.e., we can also use this inverse to perform a deconvolution of the migrated image $L'd$ in order to correct the amplitudes. Due to the higher-order complexity of the modeling and migration operators, the Hessian generally cannot be inverted for directly, and iterative procedures such as the conjugate gradient (CG) or the Newton method are often used (Lambaré et al., 1992). As an alternative, we use a method suggested by Guitton (2004) to approximate the effects of the Hessian with nonstationary matching filters. Apart from a convenient implementation, the method simulates the effects of least-squares inversion at a much reduced cost compared to an iterative approach. According to Guitton (2004), this strategy is set up as follows:

- Compute a first migrated image $m_1 = L'd$.

- Compute a second image $m_2 = L'Lm_1$.

- Estimate a bank of nonstationary matching filters B_0 such that $m_1 = B_0 m_2$.

- Convolve B_0 with m_1 to arrive at an improved image $\hat{m} = B_0 m_1$.

Convolution of the nonstationary matching filters with the first migrated image is equal to so-called one-iteration least-squares migration or migration deconvolution. The forward modeling (time demigration) is given by equation 5 and represents semi-circle superposition. The DSR migration is defined in equation 4 and implies hyperbolic summation. We note that the formulation of the demigration also requires a semi-circle-type superposition for migration as only this type satisfies the correctness of the adjoint migration (Ji, 1994). However, we decided to use the hyperbolic approach instead of the semicircle method because it is computationally efficient and even accounts for some potential artifacts in the image resulting from the hyperbolic summation. These artifacts usually show up for highly dipping events and are known to be caused by operator aliasing.

In the following, we investigate the applicability of the suggested strategy of automated velocity model building and migration deconvolution in the time domain using complex synthetic and field data examples.

SYNTHETIC DATA EXAMPLE

First, we apply the presented method to the complex Sigsbee2A synthetic data. It is a constant-density acoustic dataset released in 2001 by the Subsalt Multiple Attenuation Team Joint Venture (SMAART JV (Paffenholz et al., 2002)). The SMAART JV has created several 2D synthetic data sets. One of the objectives was to better understand the imaging issues contributing to the poor signal-to-noise ratio observed subsalt in deep water environments such as the Sigsbee Escarpment in the Gulf of Mexico. Prestack data were modeled with a 2D acoustic finite-difference approach with a dominant frequency of 20 Hz. The
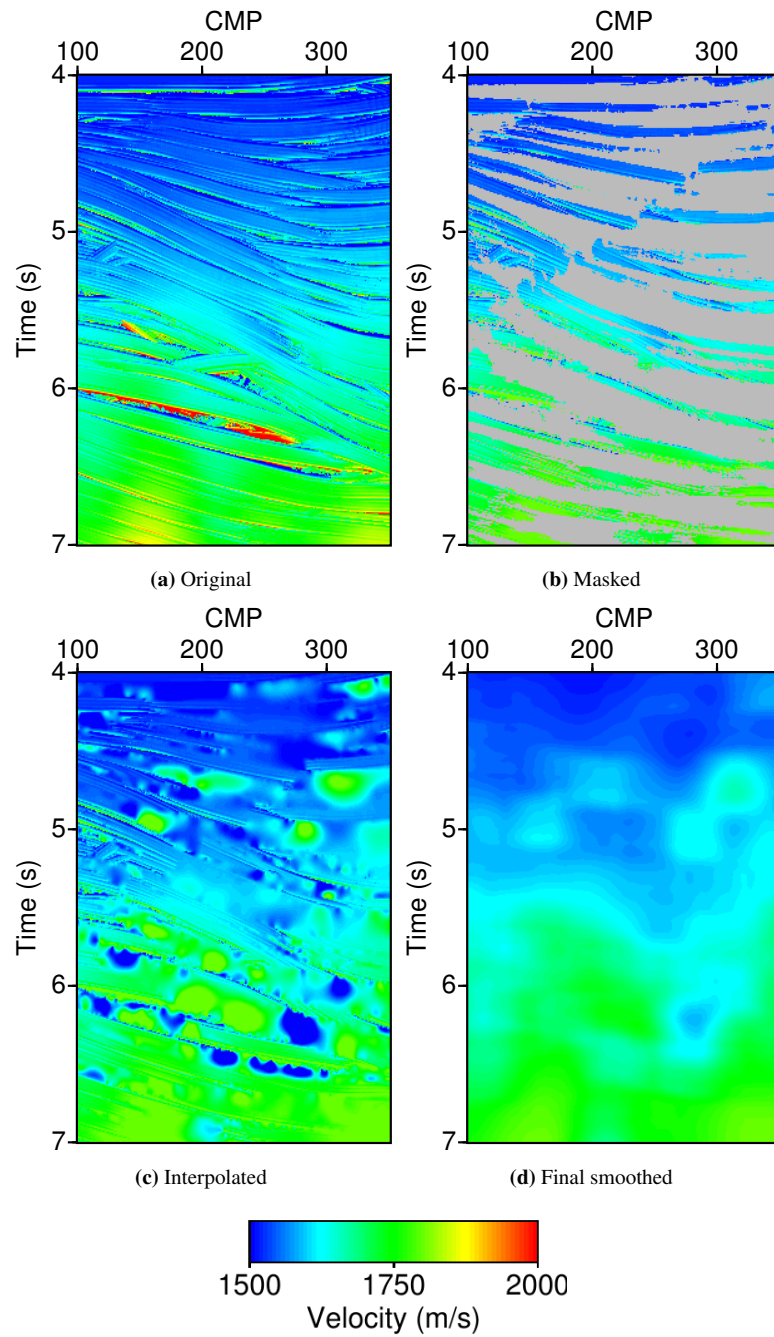
Figure 2: Synthetic data. Different steps of velocity refinement, where the colorbar applies to all images. Starting with the original velocity model (a), we masked the section with the weighted coherence (b). Afterwards, interpolation of gaps (c) and smoothing (d) is applied to obtain the refined model.

(a) Original   **(b)** Refined
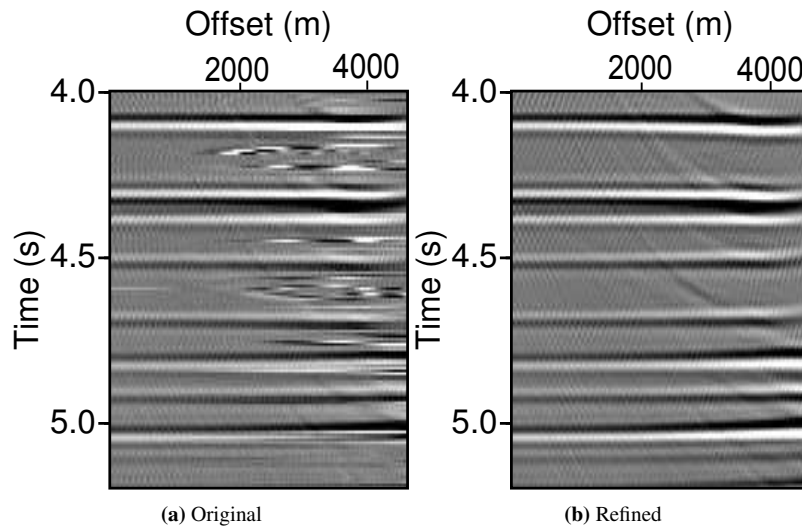
Figure 3: Synthetic data. Close-up of CIG for CMP 210. Image (a) shows the CIG with the original used velocity model. After velocity refinement is applied (b) the CIG is cleaner and more homogeneous.

CMP spacing is 11.43 m and the offset spacing is 34.29 m. The following figures show the left part of the model containing faults and diffractor lines.

Figure 2 illustrates the individual steps of the velocity refinement. Figure 2 (a) shows the original model calculated with the CRS kinematic wavefield attributes. Its structure is dominated by laterally continuous reflections, and higher as well as lower velocities are present. Higher velocities can occur because intersecting events lead to incorrect attributes and, therefore, erroneous velocities. Figure 2 (b) shows the result of the coherence filtering, performed on the initial velocity estimate. We have defined a threshold for the wavefield's semblance of the time-migrated image, which depends on the data quality. The aim is to suppress noise and keep the coherence values of the events by choosing an appropriate value of the semblance coefficient. We use this as a mask for the velocity model. Here, gray corresponds to values below the threshold. Mostly reflections due to higher amplitudes in comparison to diffractions are chosen with the coherence threshold of 0.01. Figure 2 (c) presents the result of the interpolation of the gaps from the image in Figure 2 (b). Perturbations are present where gaps in the data are comparably large, especially in the right and lower part of the image due to the interpolation. Figure 2 (d) shows the final smoothed velocity model. Additional smoothing is necessary to fulfill the requirements for time migration. This is the reason for the decreased resolution of the refined velocity model in comparison with the orignal model in Figure 2 (a).

For a further comparison of the results for the velocity refinement, Figure 3 shows common-image gathers (CIG) for CMP 210. The CIG is almost flat for the original velocity model (see Figure 3(a)). Improvements with the refinement Figure 3(b) lead to a reduction of noise at larger offsets, and a more continuous gather. The noise content for larger offsets in Figure 3(a) is due to the calculation of the original velocity model (see equation 2), which calculates the velocity for ZO with t_0 and is therefore biased for larger offsets.

In Figure 4 the migration results for the original migrated image (a), the one obtained with the refined velocity model (b), and with the migration deconvolution (c) are shown. Improvements are in particular visible in the fault area. Generally, it can be observed that our suggested strategy for time-migration velocity model building and migration deconvolution results in an improved localization and imaging of faults and a more continuous appearance of reflecting structures. Furthermore, the images of two diffractors are now better focused and clearly recognizable against the image background. For this synthetic data set the advantage of the migration deconvolution is minor, e.g. improved diffraction focusing. Here, we are pushing the limits of time-migration resolution, which is not the case for field data application. Finally, note that the improved velocity model building and the migration deconvolution were performed in a fully automated fashion.
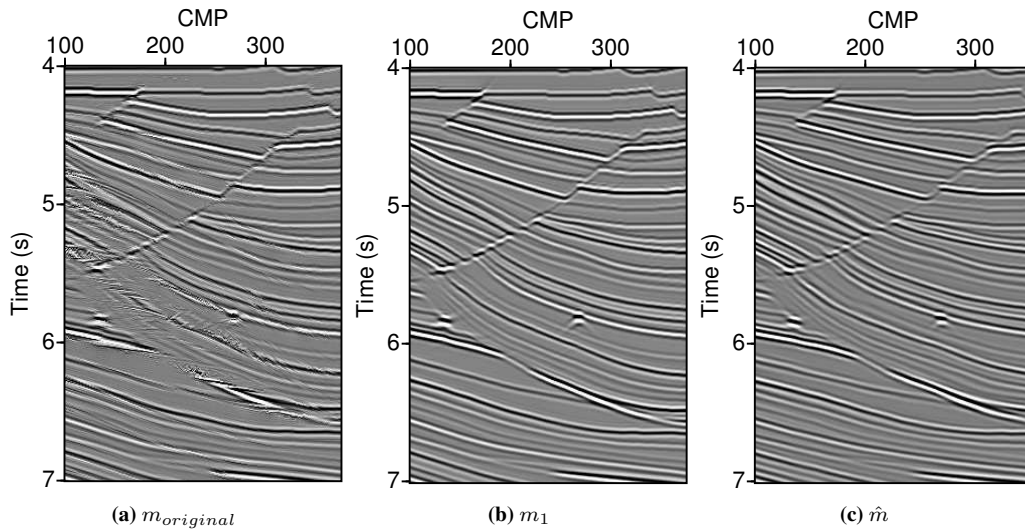
Figure 4: Synthetic data. Different migrated sections. The first image (a) shows the migration result with the original used velocity model. Velocity refinement (b) and migration deconvolution (c) improve the image quality.

FIELD DATA EXAMPLES

We applied the proposed velocity enhancement and migration/demigration loop to a marine and a land data example. The first data set was acquired by TGS in the Levantine basin in the eastern Mediterranean Sea. The Levantine Basin shows a complex seismic stratigraphy of the basinal succession. The deformation patterns of the intraevaporitic sequences include folds and thrust faulting, which provides evidence for extensive salt tectonics and shortening during the depositional phase. Previous works have shown that postdepositional gravity gliding caused salt rollers in the extensional marginal domain, as well as compressional folds, and faults within the Levantine Basin (Netzeband et al., 2006). A subset of the data consisting of around 2000 common midpoint (CMP) gathers with a total line length of approximately 25 km, a shot/receiver spacing of 25 m, a CMP spacing of 12.5 m, and maximum offsets of 7325 m was chosen. The maximum CMP fold corresponds to about 120 traces. The record length was 8 s with a 2-ms sample rate.

Figure 5 shows the different steps of the velocity refinement for a subset of the data. Figure 5 (a) shows the original velocity distribution calculated from the CRS wavefront attributes. The sedimentary layering is visible, and interrupted by the first ocean-bottom multiple. The image in Figure 5 (b) shows the velocity model after application of the coherence filter with a threshold of 0.005. Here, gray corresponds to values below the threshold. In the following step, the interpolation is executed and the result is shown in Figure 5 (c). Perturbations caused by the interpolation are less in comparison with the synthetic data due to the more homogeneous distribution of events after filtering. A final smoothing (Figure 5 (d)) of the interpolated velocities has to be carried out to perform time migration.

Figure 6 shows an overlay plot of the automatically generated velocity model and the prestack time-migrated image. The velocity model obtained by coherence filtering and interpolation is smooth and the velocities increase with time except for the first ocean-bottom multiple, which produces lower velocities at larger times, between 2 and 3 s in the lower left corner. The white and red colors indicate higher salt velocities for the triangular structures. There is noticeable consistency of the velocity model with the migrated section not only for the sedimentary layering but also for faults, which start from the triangular structures and continue to the sea floor. The sedimentary layering is horizontally ruptured by a chaotic pattern, which coincides with a slid slump complex (Hübscher and Netzeband, 2007). We also observe low velocities on the bottom of the model. These are likely caused by ocean-bottom multiples which were picked by our unconstrained automatic velocity update.

To evaluate the results of the demigration, we compare common-offset sections of the original and the
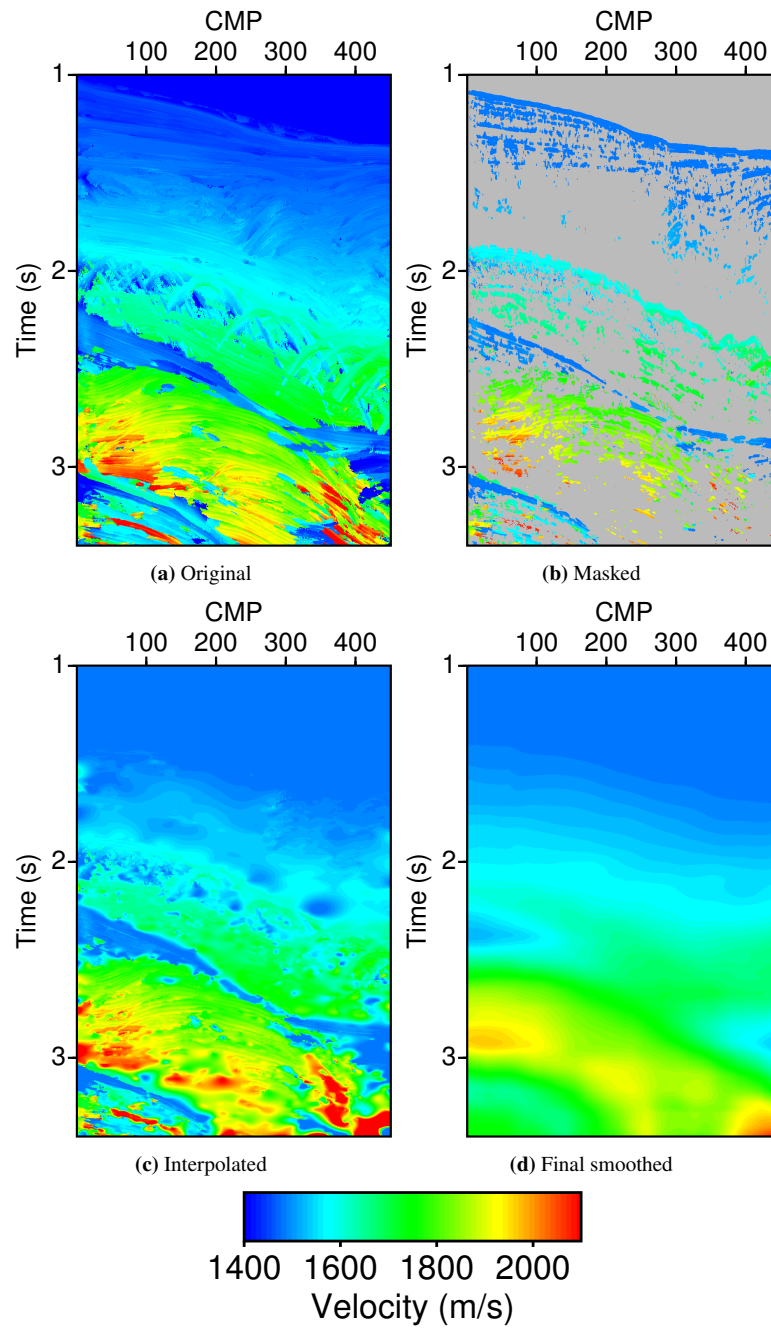
Figure 5: Marine data. Different steps of velocity refinement, where the colorbar applies to all images. Starting with the original velocity model (a), we masked the section with the weighted coherence (b). Afterwards, interpolation of gaps (c) and smoothing (d) is applied to obtain the refined model.
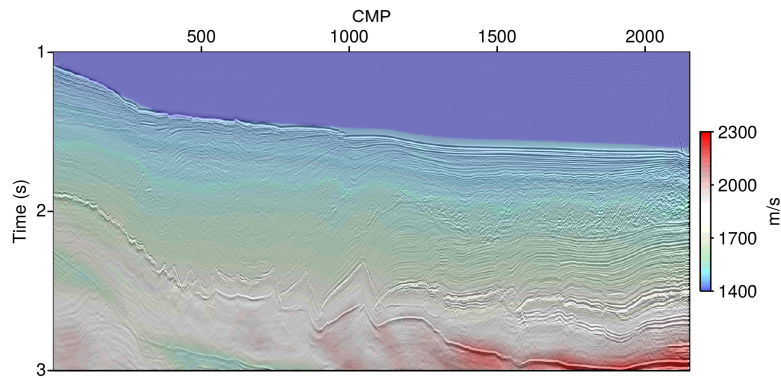
Figure 6: Marine data. An overlay plot of the refined velocity model and the corresponding prestack time-migrated section.
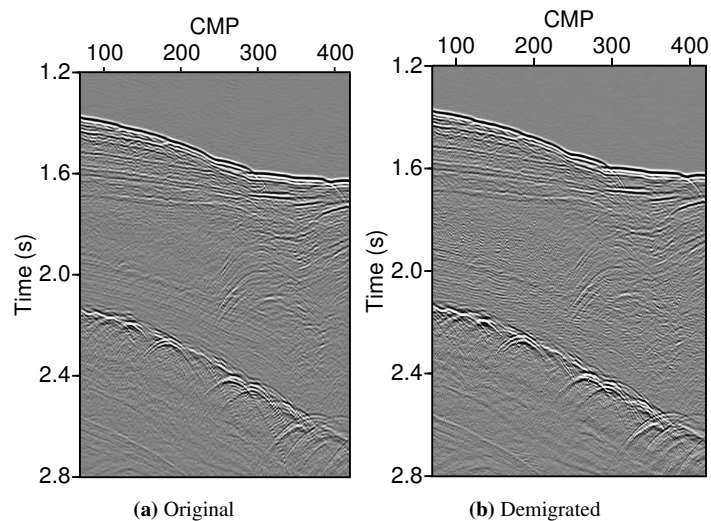
Figure 7: Marine data. Close-up of common-offset sections: original data (a) and demigrated data (b). Main events are recovered in demigrated image (b).

demigrated data. Following Hubral et al. (1996), we choose the same apertures and velocity models for forward and backward transformation. The midpoint aperture ranges from 1500 m to 2500 m and the offset aperture from 1000 m to 7000 m. Figure 7 shows common-offset sections for $h = 1000$ m, where the original data is presented on the left and the demigrated data on the right. The demigration enhances the data quality and the events are imaged with improved continuity. The second dipping reflection, starting at 1.8 s and the connected diffraction events are both enhanced. Furthermore, structures below this reflection are more visible in the demigrated section. The first ocean-bottom multiple (approximately 2.2 s at CMP 90) is more pronounced too, but reflections below, which are masked in the original data section, become clearly visible in the demigrated section. The automated scheme was able to reconstruct the original data, and improved the resolution of deeper events.

As the demigration results appear to be reasonable, we can apply the described migration deconvolution. Figure 8 shows a close up of two migrated sections. The conventional migration result m_1, i.e., the first image in our deconvolution workflow and the updated migration result $\hat{m}$, i.e., the first image convolved with the inverse of the Hessian, are shown on the left and right, respectively. Note a clearly observable wavelet shortening, i.e., deconvolution, in the updated migration result. We also see an improvement in
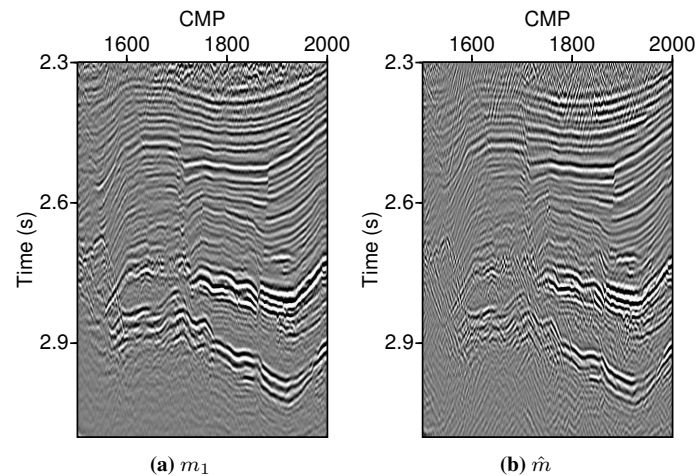
Figure 8: Marine data. Close-up of the migrated sections. Migrated image is shown in (a). The image in (b) calculated with migration deconvolution shows an improved resolution for the middle part.

focusing of diffractions and a better unfolding of bow-ties. Figure 9 displays the remigrated image m_2, i.e., the second image in the deconvolution workflow (a) and the estimated nonstationary matching filters (b). The filter seems to follow the structure – an observation that was also made by Guitton (2004) for the depth case. In time migration, however, a heavily smoothed velocity model is used. Therefore, this is an unexpected feature and confirms an appropriate velocity model. Figure 10 displays frequency spectra for the migrated (blue) and the updated (red) image. We observe an expected slight broadening of the spectrum. We also see an unexpected spectrum behavior in the updated image, namely that frequencies higher than 90 Hz, which were artificially boosted by the application of a deconvolution during the processing, became noticeable weaker.

(a) Remigrated   **(b)** Filter
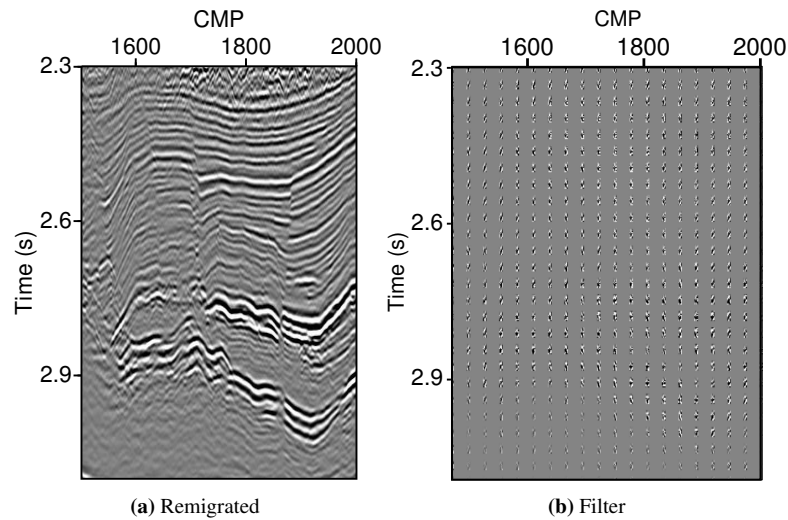
Figure 9: Marine data. Close-up of the remigrated section (a) and the estimated filters (b), where the filter follow the structures.
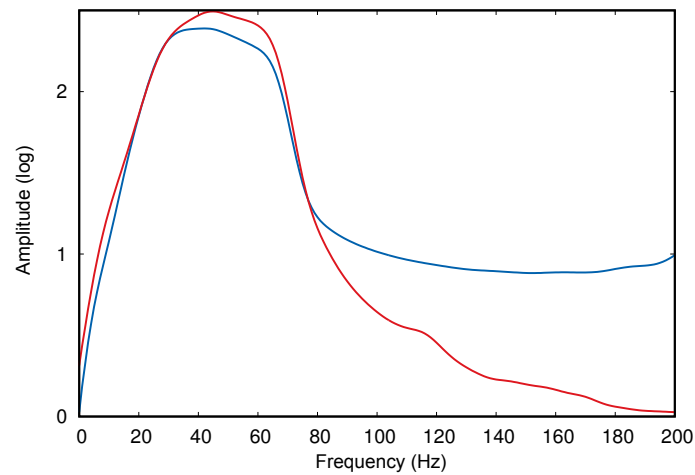

Figure 10: Marine data. Frequency spectrum corresponding to the migrated (blue) and the updated (red) image. We observe an expected slight broadening of the spectrum. We also see an unexpected spectrum behavior in the updated image, namely frequencies higher than 90 Hz, which were artificially boosted by the application of a deconvolution during processing, are weakened.

Our second data example is a land data example acquired north of the river Elbe in Northern Germany. It almost coincides with the so called Elbe-Line, and crosses the Central Triassic Graben and its deepest part, i.e., the Glückstadt Graben, perpendicular to the graben axis. Salt structures and complex fault systems characterize the region. The sedimentation process started in the Upper Rotliegend and continued to the evaporites of the Zechstein Group, which reached up to 800 m in thickness. Different phases of salt movements that started in Triassic time formed the salt structures of the region. Each phase is characterized by changing tectonic regimes and different kinds of salt diapirism (Baykulov et al., 2009). The dataset consists of 771 shot gathers with a recording length of 13 s and a sample interval of 2 ms. Explosive sources were used with an average shot spacing of 120 m. For every shot gather, 120 channels with a receiver group spacing of 40 m were deployed. Irregular shooting geometry led to a varying CMP fold, with an average value of 20. A CRS-based data enhancement was applied to the CMP data during the reprocessing in 2007. The CRS-conditioned gathers were used as migration input. In our tests we focused on sedimentary structures and salt plugs, i.e., we mainly considered the time interval from 0 to 6 s two-way traveltime (TWT). We note that the chosen part of the data includes a very complex near-surface region, i.e., in addition to the salt structures, the suggested scheme is confronted with severe weathering effects

As before, the different steps of the velocity refinement are shown in Figure 11. We display the shallow part of the flank of a salt diapir. Figure 11 (a) shows the calculated velocities determined by wavefront attributes. Higher velocities are present in the salt diapir, whereas lower velocities are visible at the flanks. The threshold value for the coherence filtering is 0.01 for this data set shown in Figure 11 (b). We fixed the near-surface velocity, which was estimated by the processing company, to obtain information for the upper part as well. Small perturbations caused by the interpolation are visible in Figure 11 (c). The continuation of layers towards the diapir is still visible. The refined velocity model after a final smoothing is shown in Figure 11 (d).

Figure 12 shows the first migrated image m_1 (a) and the second image m_2 (b). It displays a close-up including a complex salt intrusion which almost reaches the acquisition surface, thereby causing complex fault structures in the shallow part of the sections.

In Figure 13 the results of migration m_1 (a) and migration deconvolution $\hat{m}$ (b), respectively, are displayed. We notice an increase in resolution. In the near-surface area, we also observe recovery of the weathered layers after migration deconvolution. On the contrary, and as expected, the near-surface reflections after migration are widely destroyed. Somewhat unexpectedly, we observe a recovery of events in the salt region. Figure 14 shows frequency spectra corresponding to the migrated (blue) and the updated (red) image. We observe that the frequency content remains almost the same, with a slight boost of high frequencies between 60 and 120 Hz on the updated image $\hat{m}$. This is an expected behavior due to migration deconvolution.
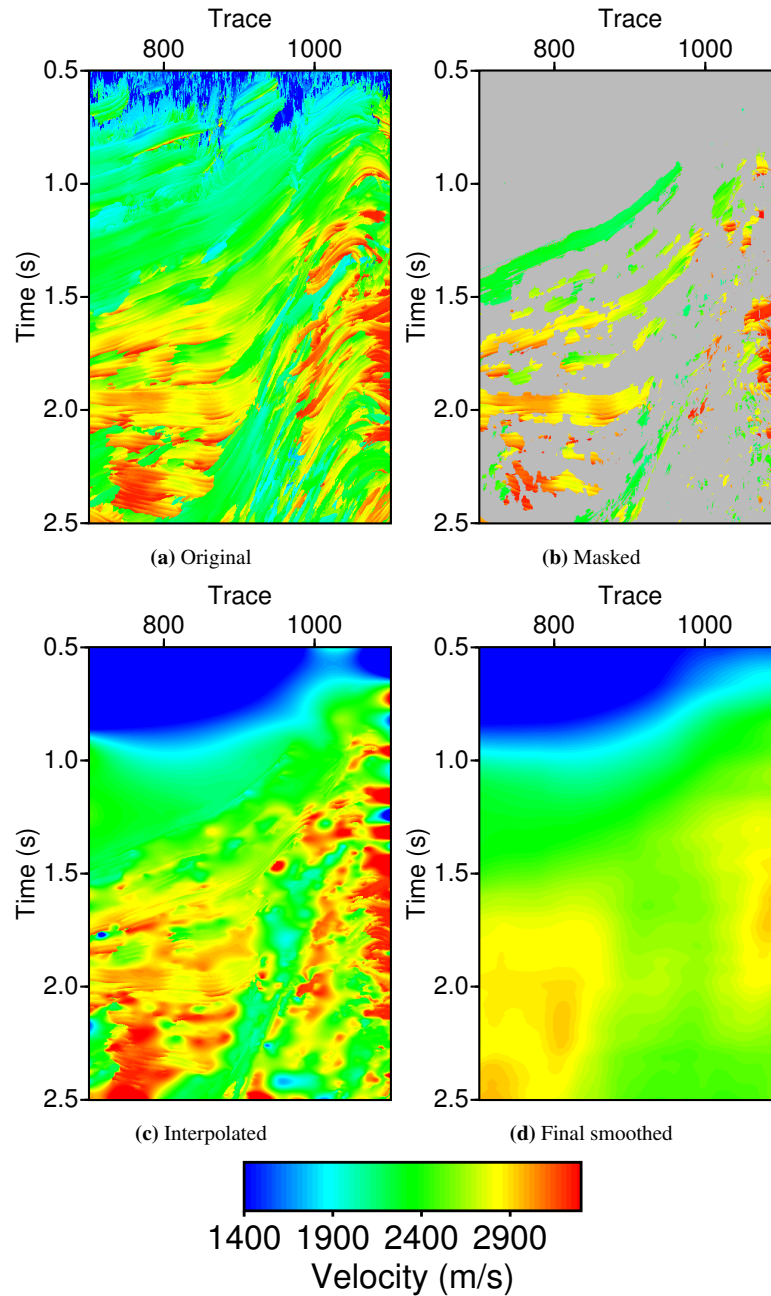
Figure 11: Land data. Different steps of velocity refinement, where the colorbar applies to all images. Starting with the original velocity model (a), we masked the section with the weighted coherence (b). Afterwards, interpolation of gaps (c) and smoothing (d) is applied to obtain the refined model.
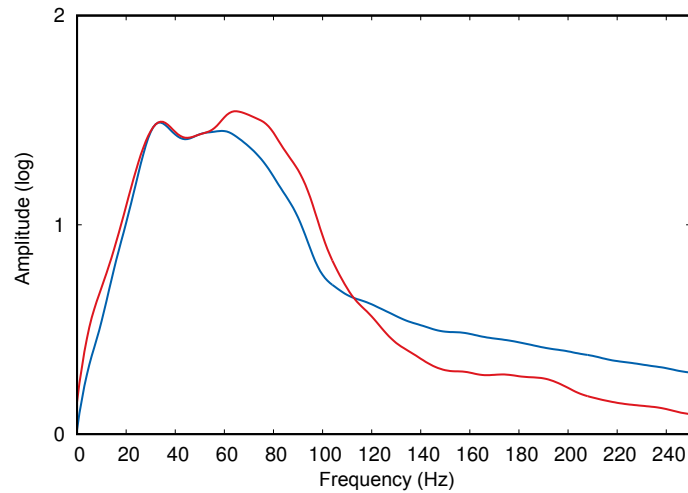
(a) Migrated image m_1 **(b)** Remigrated image m_2
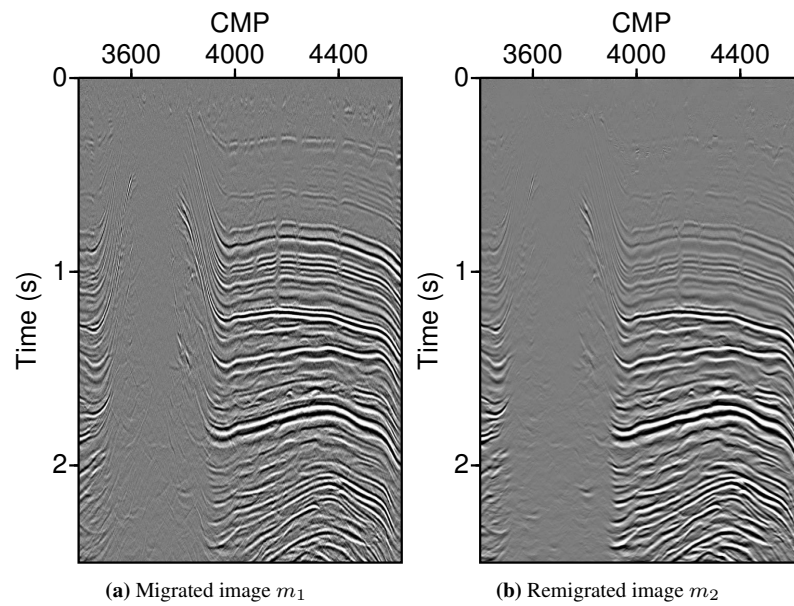
Figure 12: Land data. Close-up of the migrated image m_1 (a) and the second (remigrated) image m_2 (b) including the salt diapir.

(a) m_1 **(b)** $\hat{m}$
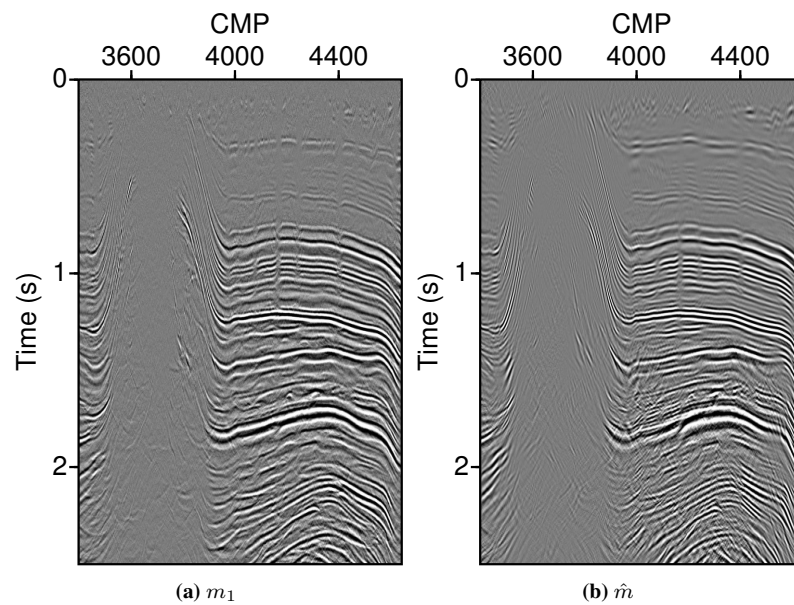
Figure 13: Land data. Result of migration (a) and migration deconvolution (b). We clearly observed an improvement in the event continuity, particularly for near-surface region and somewhat unexpected diapir region. We also recognize a noticeable deconvolution of migrated reflections.

Figure 14: Land data. Frequency spectrum corresponding to the migrated image (blue) and the updated image (red). We observe a slight boost of low and high, between 80 and 120 Hz, frequencies due to migration deconvolution.

DISCUSSION

In this section, we broadly discuss the advantages of the presented time-imaging sequence and address some issues we faced in the process. We recognize that the presented workflow belongs to the family of time-imaging methods, which may reduce its applicability to complex geological systems. However, time imaging is still present in the industry and several attempts have been made to improve it, e.g., by incorporating ray-tracing, extending Kirchhoff migration to higher (up to sixth-order) terms to better account for complex ray paths caused by heterogeneity or anisotropy, application of depth-to-time conversion where depth migration with a well-defined model is performed first and depth images are subsequently converted back to time. In this paper, we firstly addressed the model building of time-migration velocities. The conventional model-building workflow still utilizes seismic reflections only, as time migrations are usually obtained from already existing NMO velocities or through conversion from depth models. Neither of the conventional methods considers diffractions in the modeling, whereas we naturally acknowledge them in this work by utilizing kinematic wavefield attributes extracted for both reflected and diffracted events. We extract the attributes by means of a high-resolution multidimensional, multiparameter data analysis, i.e., we estimate attributes for every data point. A challenge is to determine an appropriate attribute 'de-noising' which is required to obtain smooth velocity models. The use of the coherence filter suggested in this paper may lead to an undesired neglect of weak diffracted contributions in the velocity model building process. Therefore, a careful choice of filter set-ups is required.

One of the drawbacks of time imaging is a transmission imprint on the recorded amplitudes due to the complex wave propagation through the overburden. It can be argued that seismic images (whether in depth or time) are usually not properly recovered by ray-based migration techniques. Only a full-wave migration based on at least a visco-acoustic engine will be capable of performing frequency-dependent phase and amplitude correction of the deteriorated seismic data. Moreover, because of imperfect acquisition, i.e., irregular acquisition sampling, finite recording apertures, and aliased seismic data, a least-squares migration is needed to achieve a better matching of amplitudes in the images. Visco-acoustic least-squares RTM, however, is still not a standard migration algorithm in the industry. The applied migration-deconvolution strategy will certainly not remove all undesired effects of wave propagation. However, we argue that it can help mitigate those effects which are related to imperfect acquisition and incorrect velocity models.

Furthermore, we apply LSM techniques and improve the resolution of images obtained using the approach described above. Least-squares migration involves a linear modeling/demigration operator L and its conjugate transpose migration operator L'; L operates on model m and L' operates on data d (Nemeth et al., 1999). If L is considered to be Born modeling, L is a volume integral: each contribution to the

integral expresses propagation delay from a source to a scatterer (velocity perturbation) to a receiver, followed by bandpass and derivative filtering (e.g., equation 3.2.12 of Bleistein et al. (2001), specialized to zero offset). If L is Kirchhoff modeling, L is a sum of integrals over reflecting surfaces; each contribution expresses propagation delay from a source to a reflecting surface to a receiver, also followed by bandpass and derivative filtering (e.g., equation 5.1.50 of Bleistein et al., 2001).

For both Born and Kirchhoff modeling, L and L' can be discretized as matrices. The cascade of summation and filtering means that (demigration) L is the product of matrices: $Lm = L_1 L_2 m$, where L_1 denotes filtering and L_2 denotes summation of the scattering contributions. For migration, conjugate transposition requires that $L'd = L'_2 L'_1 d$. That is, bandpass and derivative filtering are applied last in modeling and first in migration. This is important for least-squares time migration.

CONCLUSIONS

We presented a time-imaging method based on a migration/demigration loop. The method comprises an automatic model building (time-migration velocities) and an update of the migrated image (reflectivity). The basis for the forward (modeling) and backward (migration) transformation between different domains is a re-parametrized implicit common-reflection-surface (CRS) approach, which we rewrite in apex coordinates. Exploiting the implicit CRS also allows us to use kinematic wavefield attributes extracted during the high-resolution CRS-parameter analysis.

The benefits of the migration/demigration loop are that seismic data become regularized and enhanced. Moreover, conflicting event dips arising from wavefield interference are naturally handled correctly as migration repositions/removes the dips and the subsequently applied demigration restores them. To further improve the velocity model, we propose to incorporate the coherence section provided by the migration into the model-building process. A coherence threshold is selected and serves as a mask to filter the velocity model which is subsequently interpolated and smoothed. The presented method enhances the velocity models not only in areas assigned to the prominent reflections but also in the vicinity of weaker diffractions.

The duality of migration/demigration operators allows to the formulate time-migration as a least-squares problem. We directly approximate the inverse of the Hessian by nonstationary matching filters. The inverse of the Hessian is then convolved with the migrated image which yields a deconvolved migrated image, i.e., the desired least-squares estimate of the reflectivity model. We do not make any major model assumptions and perform velocity model building and the migrated-image update in a data-driven fashion. Therefore, minimal user interaction is required to carry out both the model and image update. Applications to complex synthetic and field data, acquired off-shore and on land, suggest that the proposed method is capable of noticeably reducing migration swings and recovering amplitudes, thereby leading to improved subsurface imaging in time.

ACKNOWLEDGMENTS

APPENDIX

Vanelle et al. (2010) introduced the implicit common-reflection surface (CRS) stacking approach. The approach is model-based and assumes a circle in the subsurface on which the reflection point $(R \sin \theta, H - R \cos \theta)$ is determined (see Figure 15). The traveltime is the sum of t_s, from the source to the reflection
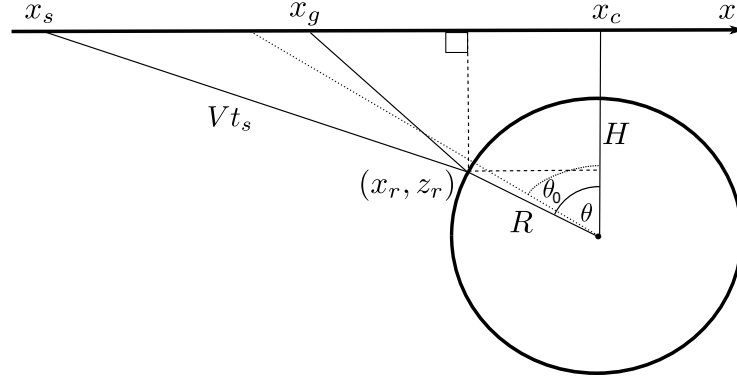
Figure 15: Implicit CRS geometry (Schwarz et al., 2014) in source-receiver coordinates. The reflection point is (x_r, z_r). The circle is described by its center point (x_c, H) and the radius R. The dottet lines inidicate the ZO case and denote the starting value θ_0 for the iterative search of the angle θ.

point, and t_g, from the reflecection point to the receiver respectively.

$$t = t_s + t_g, \quad where \tag{9}$$

$$t_s = \frac{1}{V}\sqrt{(x_s - x_r)^2 + z_r^2}, \tag{10}$$

$$t_g = \frac{1}{V}\sqrt{(x_g - x_r)^2 + z_r^2}. \tag{11}$$

We can solve these equations with the circle equation $(x_r - x_c)^2 + (H - z_r)^2 = R^2$, a fix middle point x_c, H, and a constant radius R, so that:

$$x_r = x_c + R\sin\theta \quad and \quad z_r = H - R\cos\theta. \tag{12}$$

Now equation 9 reads:

$$t = t_s + t_g, \quad where \tag{13}$$

$$t_s = \frac{1}{V}\sqrt{(x_s - x_c - R\sin\theta)^2 + (H - R\cos\theta)^2}, \tag{14}$$

$$t_g = \frac{1}{V}\sqrt{(x_g - x_c - R\sin\theta)^2 + (H - R\cos\theta)^2}, \tag{15}$$

The velocity V is constant. The reflector radius of curvature is R, H denotes the depth to the centre of the circle, and x_c describes the horizontal coordinate of the centre of the circle. It is convenient to change coordinates from source-receiver to midpoint and half-offset with $x_m = \frac{x_g + x_s}{2}$ and $h = \frac{x_g - x_s}{2}$. The reflection traveltime in common midpoint and half-offset coordiantes is:

$$t = t_s + t_g, \quad where \tag{16}$$

$$t_s = \frac{1}{V}\sqrt{(x_m - h - x_c - R\sin\theta)^2 + (H - R\cos\theta)^2}, \tag{17}$$

$$t_g = \frac{1}{V}\sqrt{(x_m + h - x_c - R\sin\theta)^2 + (H - R\cos\theta)^2}. \tag{18}$$

The angle θ is determined by an iterative solution scheme. Therefore, we have to set $\frac{\partial t}{\partial \theta} \overset{!}{=} 0$ with the solution:

$$\tan\theta = \frac{x_m - x_c}{H} + \frac{h}{H}\frac{t_s - t_g}{t_s + t_g}. \tag{19}$$

We observe that we need the angle θ for the calculation of θ. We start with the angle for the ZO case $\tan\theta_0 = \frac{x_m - x_c}{H}$ as first guess for the recursive application and are able to solve equation 16.

In order to derive a summation time-migration operator, we consider diffractions, where the implicit CRS parameter R vanishes. Accordingly, the diffraction traveltime reads as follows,

$$t_D = \frac{1}{V}\sqrt{(x_m - h - x_c)^2 + H^2} + \frac{1}{V}\sqrt{(x_m + h - x_c)^2 + H^2}. \tag{20}$$

We now parametrize equation 20 in apex coordinates. This can be achieved by minimizing the diffraction traveltime

$$\frac{\partial t_D}{\partial x_m} = 0, \tag{21}$$

with the condition of $h = 0$. The extremum,i.e., the apex is located at $x_m = x_c$ and $t_D = 2H/V$ with the resulting apex coordinates,

$$x_{apex} = x_c, \quad and \quad t_{apex} = \frac{2H}{V}, \tag{22}$$

which lead to the time-migration equation in apex coordinates,

$$t = \sqrt{\frac{t_{apex}^2}{4} + \frac{(\Delta x_a - h)^2}{V^2}} + \sqrt{\frac{t_{apex}^2}{4} + \frac{(\Delta x_a + h)^2}{V^2}}, \tag{23}$$

where $\Delta x_a = x_m - x_{apex}$ is the midpoint displacement.

REFERENCES

Baykulov, M., Brink, H. J., Gajewski, D., and Yoon, M. K. (2009). Revisiting the structural setting of the Glueckstadt Graben salt stock family, North German Basin. *Tectonophysics*, 470(1-2):162–172.

Bleistein, N., Cohen, J., and Stockwell Jr., J. (2001). *Mathematics of Multidimensional Seismic Imaging, Migration, and Inversion*. Springer Verlag, New York.

Claerbout, J., Green, C., and Green, I. (1996). *Imaging the Earth's Interior*. Free Software Foundation.

Dell, S., Gajewski, D., and Vanelle, C. (2012). Prestack time migration by common-migrated-reflector-element stacking. *Geophysics*, 77(3):S73–S82.

Gloeckner, M., Schwarz, B., Vanelle, C., and Gajewski, D. (2016). Kinematic time demigration with an automatically generated velocity model. *78th EAGE Conference and Exhibition*. Expanded Abstract.

Guitton, A. (2004). Amplitude and kinematic corrections of migrated images for nonunitary imaging operators. *Geophysics*, 69(4):1017–1024.

Hertweck, T., Jäger, C., Goertz, A., and Schleicher, J. (2003). Aperture effects in 2.5D Kirchhoff migration: A geometrical explanation. *Geophysics*, 68:1673–1684.

Hu, J., Schuster, G. T., and Valasek, P. (2001). Poststack migration deconvolution. *Geophysics*, 66:939–952.

Hubral, P. (1983). Computing true amplitude reflections in a laterally inhomogeneous earth. *Geophysics*, 48:1051–1062.

Hubral, P., Schleicher, J., and Tygel, M. (1996). A unified approach to 3-D seismic reflection imaging, Part I: Basic concepts. *Geophysics*, 61(3):742–758.

Hübscher, C. and Netzeband, G. (2007). Evolution of a young salt giant: The example of the Messinian evaporites in the Levantine Basin. *In: Wallner, M., Lux, K.-H., Minkley, W., Hardy, Jr., H.R. (Eds.) The Mechanical behaviour of Salt - Understanding of THMC Processes in Salt*, pages 175–184.

Iversen, E., Tygel, M., Ursin, B., and de Hoop, M. (2012). Kinematic time migration and demigration of reflections in pre-stack seismic data. *Geophysical Journal International*, 189:1635–1666.

Jäger, R., Mann, J., Höcht, G., and Hubral, P. (2001). Common-reflection-surface stack: Image and attributes. *Geophysics*, 66:97–109.

Ji, J. (1994). Toward an exact adjoint: Semicircle versus hyperbola. *Stanford Exploration Project*, SEP-80:499âĂŞ512.

Lambaré, G., Virieux, J., Madariaga, R., and Jin, S. (1992). Iterative asymptotic inversion in the acoustic approximation. *Geophysics*, 57:1138–1154.

Müller, T. (1999). *The Common Reflection Surface stack method - Seismic imaging without explicit knowledge of the velocity model*. PhD thesis, University of Karlsruhe.

Neidell, N. and Taner, T. (1971). Semblance and other coherency measures for multichannel data. *Geophysics*, 36:482–497.

Nelder, J. and Mead, R. (1965). A simplex method for function minimization. *Computer Journal*, 7:308–313.

Nemeth, T., Wu, C., and Schuster, G. T. (1999). Least-squares migration of incomplete reflection data. *Geophysics*, 64:208–221,DOI:10.1190/1.1444517.

Netzeband, G., Gohl, K., Hübscher, C., Ben-Avraham, Z., Dehgahni, A., Gajewski, D., and Liersch, P. (2006). The Levantine Basin - crustal structure and origin Messinian evaporites in the Levantine Basin. *Tectonophysics*, 418:178–188.

Paffenholz, J., Stefani, J., Mclain, B., and Bishop, K. (2002). Sigsbee2a Synthetic Subsalt Dataset - Image Quality as Function of Migration Algorithm and Velocity Model Error. *64th EAGE Conference and Exhibition*. Expanded Abstract.

Schuster, G. (1993). Least-squares crosswell migration. *63th Annual International Meeting, SEG*, page 110âĂŞ113. Expanded Abstracts.

Schwarz, B., Vanelle, C., Gajewski, D., and Kashtan, B. (2014). Curvatures and inhomogeneities: An improved common-reflection-surface approach. *Geophysics*, 79(5):S231–S240.

Tygel, M., Schleicher, J., and Hubral, P. (1996). A unified approach to 3-D seismic reflection imaging, Part II: Theory. *Geophysics*, 61(3):759–775.

Vanelle, C., Kashtan, B., Dell, S., and Gajewski, D. (2010). A new stacking operator for curved subsurface structures. *80th Ann. Internat. Mtg. Soc. Expl. Geophys.* Expanded Abstracts.

Walda, J., Schwarz, B., and Gajewski, D. (2017). A competitive comparison of multiparameter stacking operators. *Geophysics*, 82(4):V275–V283.

Yilmaz, O. (2001). *Seismic Data Analysis*. SEG, Tulsa.

Yilmaz, O. and Claerbout, J. F. (1980). Prestack partial migration. *Geophysics*, 45:1753–1779.